Article

Not peer-reviewed version

Sensorless Control of SPM Motor for e-Bike Applications

Abdin Pasund *, Pierfrancesco Sartori, Nicola Bianchi

Posted Date: 24 October 2024

doi: 10.20944/preprints202410.1826.v1

Keywords: field oriented control; second order generalized integral flux observer; Park transformation; Clarke transformation; sensorless algorithm; phase locked loop; quadrature signal generator

doi:10.20944/preprints202410.1826.v1

Article

Sensorless Control of SPM Motor for e-Bike Applications

Abdin Pasund [1,*,†], **Pier Francesco Sartori** [1,†] **Nicola Bianchi** [1,†]

[1] Department of Electrical Engineering, University of Padova, 35131 Padova, Italy

* Correspondence: xxx.abdin@phd.unipd.it or abdinpasund@gmail.com

† These authors contributed equally to this work.

Abstract: The aim of this research is to present both a sensorless control and a torque derating algorithm in the overload region of a permanent magnet motor for e-bike. First the theoretical backgrounds and the field oriented control are presented. Then a sensorless control, based on the back-emf estimation with a second order generalized integral flux observer for permanent magnet motor, has been designed. The second order generalized integral flux observer is an adaptive filter which can eliminate the DC offset and strongly attenuate the harmonics of the estimated rotor flux. The algorithms have been simulated and then validated by means of tests on a permanent magnet motor for e-bike.

Keywords: field oriented control; second order generalized integral flux observer; Park transformation; Clarke transformation; sensorless algorithm; phase locked loop; quadrature signal generator

---

1. Introduction

The widespread use of Electric Vehicles (EVs) in urban areas is inevitable, as the adoption of zero-emission vehicles is becoming mandatory for well-known reasons. This transition will be gradual due to the necessary infrastructure requirements, but it is already recognized that EVs will be the future solution for urban transportation [1]. Surface-mounted permanent magnet (SPM) synchronous motors are an ideal choice for applications demanding high power efficiency. The absence of excitation currents and the high power factor make them highly competitive [2]. Electric vehicles used in urban transportation require immediate and highly effective control to prevent any undesirable situations [3]. In sensored Field Oriented Control (FOC) the rotor position information is provided by a mechanical sensor, which leads to a higher cost and lower reliability [4]. Accurate rotor position is required for both open-loop and closed-loop control. Shaft-mounted sensors face challenges such as mechanical faults, decreased operational reliability, uneven placement of position sensors, and operational failures [5]. However, the mechanical sensors can be replaced with a sensorless algorithm that provides rotor position and speed. The sensorless motor control algorithm is a compelling research area in the motor drive sector. Although motor position sensors are still widely used in most industrial motor drives, cost considerations are driving the industry to eliminate them. Additionally, mounting position sensors on machines is often problematic, especially in specific applications. For instance, in outer rotor machines with limited space, attaching the position sensor to the outer cup rotor is challenging. In drones, where the rotor blade motor is typically a small outer rotor machine, there is no room for a high-accuracy position sensor or even a simple hall sensor [6]. For medium and high speed regions, the most used sensorless algorithm are back-EMF based, where the rotor position is extracted from the fundamental wave of the back-EMF [7]. In this paper, the mathematical equations of the SPM motor in the rotating reference frame are first described. Then, FOC control system and Space Vector Modulation (SVM) technique with sensors is explained. A current loop controller with a sensorless algorithm is designed for the SPM motor based on the given specifications. The back-EMF is estimated using frequency-locked loop and phase-locked loop analysis with a Second Order Integral Flux Observer (SOIFO) filter. Finally, electromechanical speed ω_m^e and position θ_m^e are estimated using the quadrature signal generalized phase-locked loop method. A brief conclusion is drawn by analyzing the results at different loads and speeds.

2. Standard Control of SPM Motor

2.1. Permanent Magnet Synchronous Motor

The Permanent Magnet Synchronous Motor (PMSM) is described by the following equations in the rotating reference frame,

$$v_d = R_s i_d + L_d \frac{di_d}{dt} - \omega_m^e L_q i_q \tag{1}$$

$$v_q = R_s i_q + L_q \frac{di_q}{dt} + \omega_m^e L_d i_d + \omega_m^e \Lambda_m \tag{2}$$

where i_d and i_q are the phase current, v_d and v_q are the phase voltage, respectively. ω_m^e is the electromechanical speed, Λ_m is the flux linkage produced by the magnets, L_d and L_q are the d-axis and q-axis synchronous inductances and R_s is the phase resistance.

2.2. Field Oriented Control

FOC is the most used control for PMSM. For a given current, maximum torque can be achieved when the stator flux due to the stator current is orthogonal to the rotor flux, created by the PM [8]. Electromagnetic torque is a function of the angle between the stator and rotor flux. The equation that describes the average electromagnetic torque is,

$$T_{avg} = \frac{3}{2} p \Lambda_m I_q \tag{3}$$

where I_q is the quadrature current, p is the number of pole pairs. Figure 1 shows the FOC architecture. The 3-phase currents and the rotor angle are measured on motor terminals and rotor shaft respectively. The 3-phase currents are converted into a two phase vector frame, I_α and I_β, in the stationary state, using the Clarke transformation, then to the rotating reference frame using the Park transformation [9]. The currents are referred to as direct axis current, I_d, and quadrature axis current, I_q. In order to have the maximum torque for a given current, the current I_q must be fully oriented along the quadrature axis [10]. These two currents are compared to the reference values and the errors are used as input to PI regulators. The control is implemented in the steady state frame, since the currents and voltages are constant. The output of the regulators, which are the direct voltage, v_d, and quadrature voltage, v_q, undergoes the transformation to the stationary reference frame, and the α and β voltages are used to calculate the inverter duty cycle using the space vector modulation (SVM).

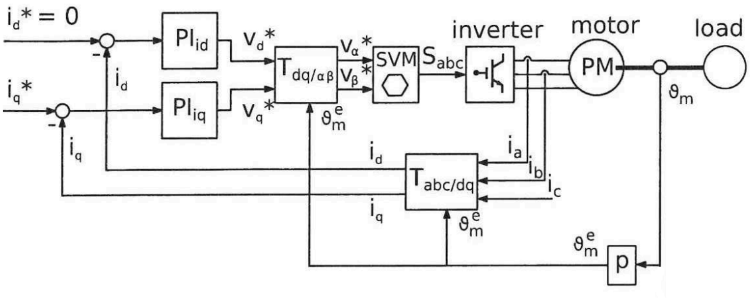

Figure 1. FOC architecture

The FOC consists in controlling the stator currents and the torque. The idea behind the operation is the transformation from a three-phase time dependent system into a two coordinate system [11].

2.3. Space Vector Modulation

SVM is a modulation technique able to generate the desired phase voltages [12]. Since only one mosfet is ON and the other is OFF in each leg, there are 8 possible combinations. The phase vectors divide the plan into 6 sectors, each spanning 60°. Depending on the sector addressing the desired phase voltage, two adjacent vectors are applied in succession. The two vectors are time weighted in a switching period T_s to produce the desired output voltage. Let's assume the desired voltage is in the first sector $(0° - 60°)$, the following condition holds

$$\overline{v} = \overline{v}_{100}\frac{t_1}{T_s} + \overline{v}_{110}\frac{t_2}{T_s} + \overline{v}_{111}\frac{t_0}{T_s} \tag{4}$$

where t_1 and t_2 are the times in which the vectors $\overline{v}_{100}$ and $\overline{v}_{110}$ are applied respectively, t_0 is the time in which the zero vector is applied. By splitting the above equation in real and imaginary parts it is

$$\begin{cases} |\overline{v}| \sin\alpha = \frac{\sqrt{3}}{2}|V|\frac{t_2}{T_s} \\ |\overline{v}| \cos\alpha = |V|\left(\frac{t_1}{T_s} + \frac{1}{2}\frac{t_2}{T_s}\right) \end{cases} \tag{5}$$

Finally, since $|V| = \frac{2}{3}V_{dc}$, the times can be written as

$$\begin{cases} t_1 = \sqrt{3}\frac{|v|}{V_{dc}} T_s \sin(\frac{\pi}{3} - \alpha) \\ t_2 = \sqrt{3}\frac{|v|}{V_{dc}} T_s \sin(\alpha) \end{cases} \tag{6}$$

3. Methodology

The algorithms have been simulated and then validated with the use of the dSpace MicroLabBox platform. SPM motor parameters are given in Table 1.

Table 1. Motor Parameters

Parameter	Symbol	Value	Unit
Pole number	$2p$	10	-
PM Flux linkage	Λ_m	0.0144	Vs
Winding resistance	R_s	0.222	Ω
Winding inductance	L_s	0.25	mH
Nominal speed	n_n	2500	rpm
Nominal torque	T_n	2	Nm

3.1. Current Loop Design

Figures 2 and 3 show the block diagrams related to the current control loop in the synchronous reference frame. If the electric motor is isotropic then $L_d = L_q$ [13]. In the control loops the term $\omega_m^e L_q i_q$ and the term $\omega_m^e L_d i_d$ has been added to u_d and u_q respectively, in order to decouple the two dynamics. If the time constant τ_c introduced by the inverter is negligible with respect to the electric time constant of the motor L_d/R_s and L_q/R_s, then the terms added to the voltages will cancel those in the motor block diagrams [14]. In order to better control the dynamic of the i_q current loop, also the term $\omega_m^e \Lambda_m$ is added to compensate the effect of the back-EMF. The open loop transfer function related to the current loop is then

$$T_{OL} = \frac{k_i + k_p s}{s}\frac{1}{R_s}\frac{1}{1 + \frac{sL}{R_s}}\frac{1}{1 + \frac{s}{\tau_c}} \tag{7}$$

The bandwidth is fixed to $f = 1kHz$ and the phase margin to 60°. The regulator gains that have been calculated from those specifications are $k_p = 1.44$ and $k_i = 4186$.

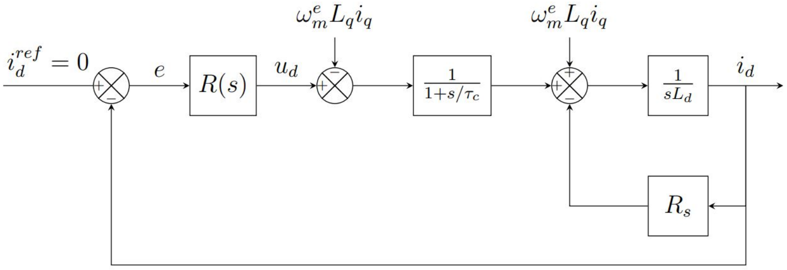

Figure 2. Simplified block scheme of i_d current loop

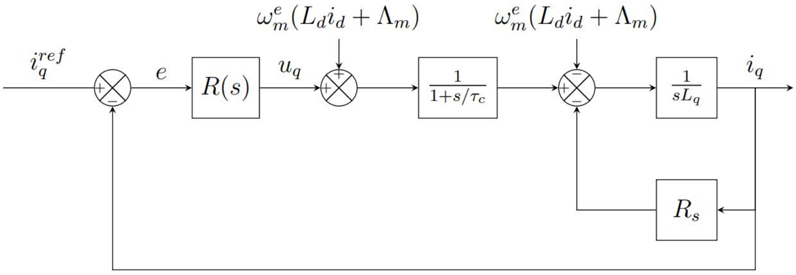

Figure 3. Simplified block scheme of i_q current loop

3.2. Sensorless Algorithm

The current and voltage are filtered and filtered-integrated by a Second Order - Second order Generalized Integrator (SO-SOGI), which is a forth order adaptive filter, and they are going to be used to estimate Λ_α and Λ_β, which will be used to extract the rotor position. The overall structure is called Second Order Integral Flux Observer (SOIFO) and has strong attenuation capability against the dc offset and harmonics.

3.2.1. Back-emf

The voltage and flux equations of a PMSM motor in $\alpha\beta$ coordinate can be described by the following equations [15].

$$\boldsymbol{u}_{\alpha_\beta} = R_s \cdot \boldsymbol{i}_{\alpha_\beta} + \frac{d}{dt}\boldsymbol{\lambda}_s = R_s \cdot \boldsymbol{i}_{\alpha_\beta} + L_s \cdot \boldsymbol{i}_{\alpha_\beta} + \Lambda_m \cdot \begin{bmatrix} \cos(\theta_m^e) \\ \sin(\theta_m^e) \end{bmatrix} \tag{8}$$

where $\boldsymbol{u}_{\alpha_\beta}$ is the stator voltage vector, $\boldsymbol{i}_{\alpha_\beta}$ is the stator current vector, $\boldsymbol{\lambda}_s$ is the stator flux vector, L_s is the stator inductance, R_s is the stator resistance, θ_m^e is the rotor electrical position and $\boldsymbol{\Lambda}_m$ is the rotor flux linkage. The PMSM sensorless control based on the rotor flux observation is shown in Figure 4, where $\hat{\theta}_m^e$ and $\hat{\omega}_m^e$ are the estimated electromechanical position and the speed.

From (8) the following equation can be obtainted

$$\boldsymbol{\lambda}_r = \int \left(\boldsymbol{u}_{\alpha\beta} - R_s \boldsymbol{i}_{\alpha\beta} - L_s \cdot \frac{d}{dt} \boldsymbol{i}_{\alpha\beta} \right) dt \tag{9}$$

The error due to the integral initial value of the estimated rotor flux is calculated as

$$\boldsymbol{\lambda}_r(0) = \boldsymbol{\lambda}_s(0) - L\boldsymbol{i}_{\alpha\beta}(0) \tag{10}$$

On top of that, other errors will be introduced due to parameters mismatch, unknown integral initial value, measurements error, inverter nonlinearities etc. Then the following equation can be obtained

$$\boldsymbol{\lambda}_r = \int \boldsymbol{u}_{\alpha\beta} dt - \int (R_s + \Delta R_s) \boldsymbol{i}_{\alpha\beta} dt - \int (L_{\alpha\beta} + \Delta L) \cdot \frac{d}{dt} \boldsymbol{i}_{\alpha\beta} dt + \int \boldsymbol{e}_{\alpha\beta 0} dt + \int \chi dt \tag{11}$$

doi:10.20944/preprints202410.1826.v1

where ΔR_s and ΔL_s are the parameter variation, $\boldsymbol{e}_{\alpha\beta 0}$ is the initial back-EMF vector and χ represents other errors.

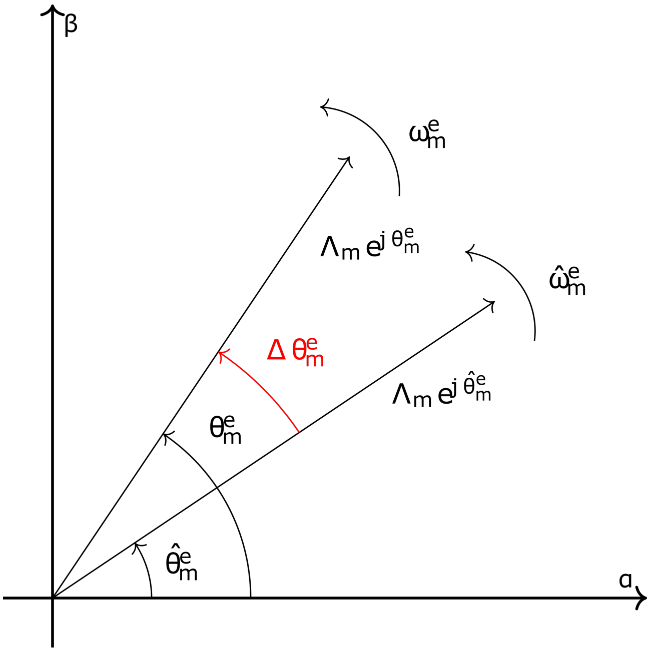

Figure 4. Rotor flux observation

3.3. Frequency Locked Loop

The frequency locked loop is a control loop used to auto-adapt the center frequency of the SOGI filter to the fundamental input frequency [16]. Figure 5 shows the architecture of the FLL. The transfer function between the error ε and the input signal is

$$E(s) = \frac{\varepsilon(s)}{v(s)} = \frac{K_1\omega' s(s^2+\omega'^2)}{[s^4+s^3(K_2\omega')+s^2(2\omega'^2+K_1K_2\omega'^2)+s(K_2\omega'^3)+\omega'^4]} \tag{12}$$

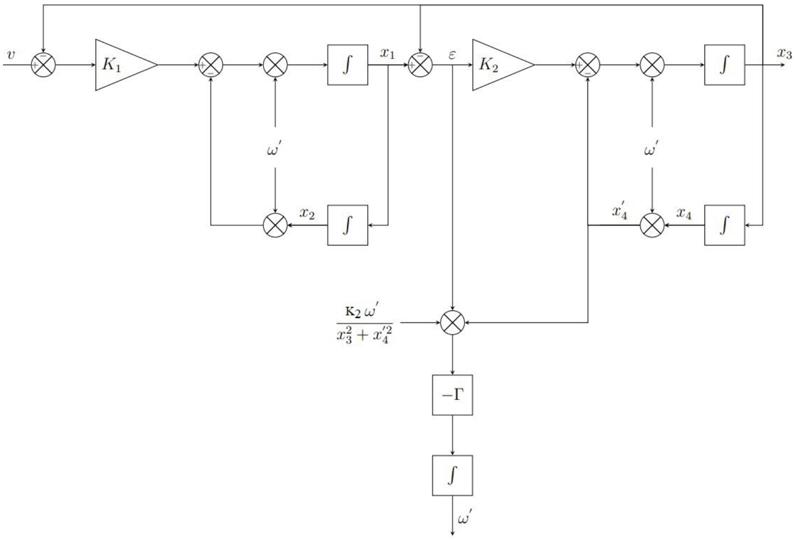

Figure 5. SO-SOGI-FLL block diagram

The transfer function is a notch filter with unity gain at the centre frequency. The phase angle of this transfer function experiences a phase jump of +180° when the frequency of the input signal ω goes from lower to higher to that of the estimated ω' of the FLL. Figure 6 shows that the transfer function $E(s)$ and $x_4^{'}(s)$ are in phase when the frequency of the input signal is lower than that of the FLL ($\omega < \omega^{'}$), and are in phase opposition otherwise ($\omega > \omega^{'}$). A new variable ε_f is defined as the product between ε and $x_4^{'}$. This variable will be positive when $\omega < \omega^{'}$, 0 when $\omega = \omega^{'}$ and negative when $\omega > \omega^{'}$. Based of these considerations, the FLL can be designed using this frequency error ε_f as the input to a negative gain $-\gamma$ and an integrator. In this way, if there is a mismatch between the input frequency and the FLL frequency, this control loop will drive the FLL frequency up to the input frequency. Also, in order to accelerate the dynamic, the centre frequency $\omega^{'}$ can be added as a feed-forward variable, since the magnitude of the input of the FLL decreases as the two frequencies differ, as shown in Figure 6.

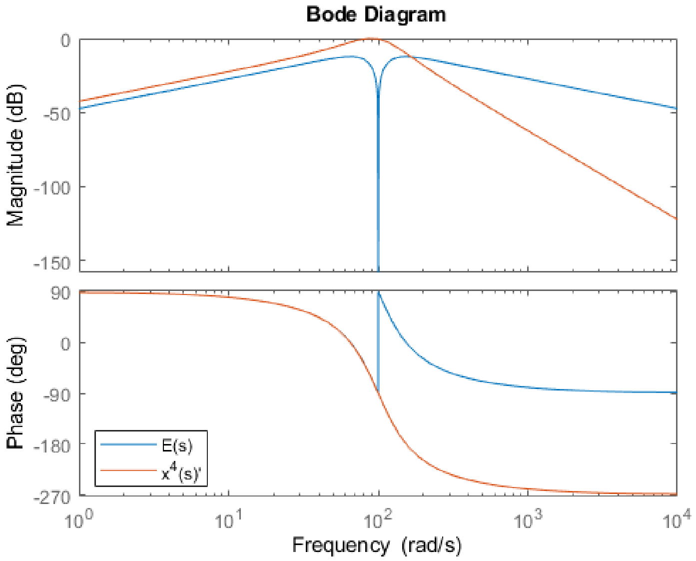

Figure 6. Bode diagrams of $E(s)$ and $x_4^{'}(s)$

3.4. Phase Locked Loop Analysis

Let's assume the input signal is given by:

$$v = V\sin(\theta) = V\sin(\omega t + \phi) \tag{13}$$

and the output signal is given by:

$$v' = \cos(\theta') = \cos(\omega' t + \phi') \tag{14}$$

then the output of the phase multiplier can be written as:

$$\varepsilon = V\sin(\omega t + \phi)\cos(\omega' t + \phi') = \frac{V}{2}[\underbrace{\sin((\omega - \omega')t + (\phi - \phi'))}_{\text{low frequency term}} + \underbrace{\sin((\omega + \omega')t + (\phi + \phi'))}_{\text{high frequency term}}] \tag{15}$$

If the PD regulator of the PLL is a multiplier it is necessary to choose the bandwidth of the system low enough to attenuate the high frequency term, and so only the DC term remains:

$$\varepsilon = \frac{V}{2}\sin((\omega - \omega')t + (\phi - \phi')) \tag{16}$$

Assuming that the V_{CO} is tuned to the input frequency, $\omega \approx \omega'$, then the PD error is further simplified into

$$\varepsilon = \frac{V}{2}\sin(\phi - \phi') \tag{17}$$

doi:10.20944/preprints202410.1826.v1

As a last step, assuming that the phase error is low, $\phi \approx \phi'$, the output of the PD regulator can be linearized in the vicinity of that operating point because $\sin(\phi - \phi') \approx \sin(\theta - \theta') \approx (\theta - \theta')$. The result

$$\varepsilon = \frac{V}{2}(\theta - \theta') \tag{18}$$

Assuming V=1, the open loop transfer function in the Laplace domain is

$$F(s)_{OL} = PD(s)LF(s)V_{CO}(s) = \frac{k_p(1 + \frac{1}{sT_i})}{s^2} \tag{19}$$

and the closed loop transfer function is

$$F(s)_{CL} = \frac{sK_p + \frac{K_p}{T_i}}{s^2 + sK_p + \frac{K_p}{T_i}} \tag{20}$$

The closed loop transfer function can be normalized in the following way

$$F(s)_{CL} = \frac{2\zeta\omega_n s + \omega_n^2}{s^2 + 2\zeta\omega_n s + \omega_n^2} \tag{21}$$

where

$$\omega_n = \sqrt{\frac{K_p}{T_i}} \quad \text{and} \quad \xi = \frac{\sqrt{K_p T_i}}{2} \tag{22}$$

The response time of this second-order system, from the start of the variation to the 99% of the steady-state final value, can be approximated through

$$t_s = 4.6\tau \quad \text{with} \quad \tau = \frac{1}{\xi\omega_n} \tag{23}$$

From (20), (21) and (23), the parameters of the controller can be tuned as follows

$$K_p = 2\xi\omega_n = \frac{9.2}{t_s} \quad \text{and} \quad T_i = \frac{2\xi}{\omega_n} = \frac{t_s\xi^2}{2.3} \tag{24}$$

3.5. Second Order Integral Flux Observer Architecture

In the SOIFO, there are four SO-SOGI-FLL that have the following quantities as input: i_α, i_β, v_α and v_β. The output of those SO-SOGI-FLL will be the filtered and the integrated filtered input. In this way, the following quantities can be computed

$$\lambda_\alpha = \int (V_\alpha - R_s i_\alpha)dt - L_s i_\alpha \tag{25}$$

$$\lambda_\beta = \int (V_\beta - R_s i_\beta)dt - L_s i_\beta \tag{26}$$

Figure 7 show the architecture of the two SOIFO, where $\hat{i}_{\alpha\beta}$ and $\hat{v}_{\alpha\beta}$ represents the filtered variables. λ_α and λ_β are used as the input of the QSG-PLL, described hereafter as shown in Figure 8, and the estimated speed $\hat{\omega}_m^e$ and estimated position $\hat{\theta}_m^e$ are obtained.

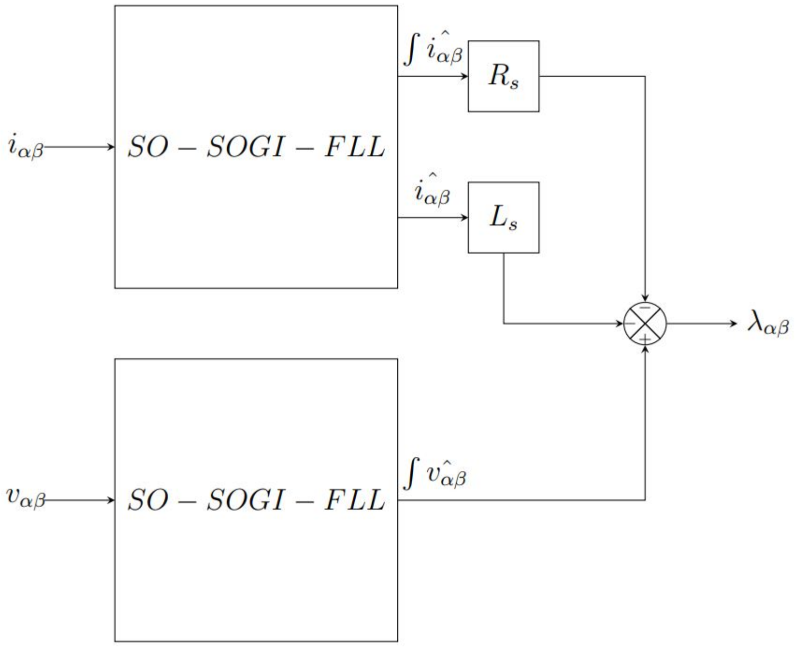

Figure 7. $SOIFO_{\alpha\beta}$

3.6. Quadrature Signal Generator - Phase Locked Loop

There is a high frequency term in the output of the phase detector. In order to attenuate the effect of this term on the angular velocity and angular position the bandwidth of the control loop must be decreased [17]. A trade-off arises, because a decrease of bandwidth leads to an increase of the settling time. Because of this, a new PLL scheme called Quadrature Signal Generator PLL (QSG-PLL) is introduced in Figure 8. Referring to Figure 8, if $v_\alpha = V\cos(\omega t + \phi)$ and $v_\beta = V\sin(\omega t + \phi)$, the new output of the phase detector can be calculated as

$$\varepsilon = V\sin(\omega t + \phi)\cos(\omega' t + \phi') - V\cos(\omega t + \phi)\sin(\omega' t + \phi') = V\sin((\omega - \omega' t) + (\phi - \phi')) = V\sin(\theta - \hat{\theta}) \tag{27}$$

where $\hat{\omega}_m^e$ and $\hat{\theta}_m^e$ are the estimated variables of the PLL. In this way, the high frequency term disappears, and the bandwidth of the control loop can be increased. Also, a normalization block is introduced to make the bandwidth of the control loop independent from the amplitude of the input signals.

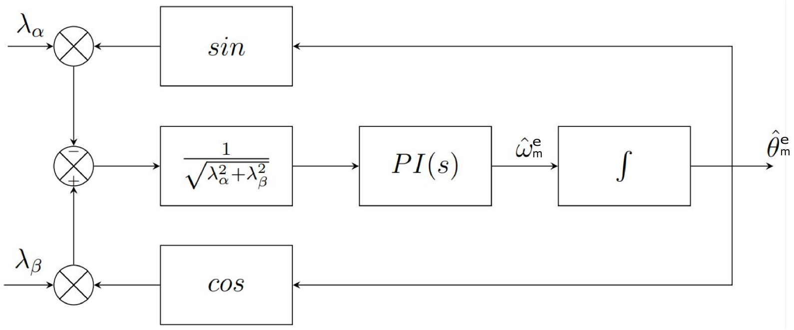

Figure 8. QSG-PLL block diagram

4. Results

The electric angular frequency of the back-EMF at which the sensorless algorithm is started has been chosen as $\omega_m^e = 25$ rad/s, which is about 48 rpm. By resorting to the design procedure explained in Section 3.3, the settling time has been chosen as $t_s = 0.1s$ and the damping ratio as $\zeta = 1/\sqrt{2}$, which

doi:10.20944/preprints202410.1826.v1

leads to an overshoot of $\sigma = 4.3\%$. The undamped natural frequency is then 62.23 rad/s. Finally, the gains mentioned in Figure 5 are computed as $K_1 = 1.76$ and $K_2 = 7.04$.

4.1. Second Order - Second Order Generalized Integrator dynamic

The SO-SOGI is simulated with $v = A\cos(\omega t)$ as input, where A = 1 and ω_m^e = 250 rad/s. Figures 9 and 10 show the results after a step amplitude variation of 20%, and Figures 11 and 12 show the results after a step frequency variation of 20%.

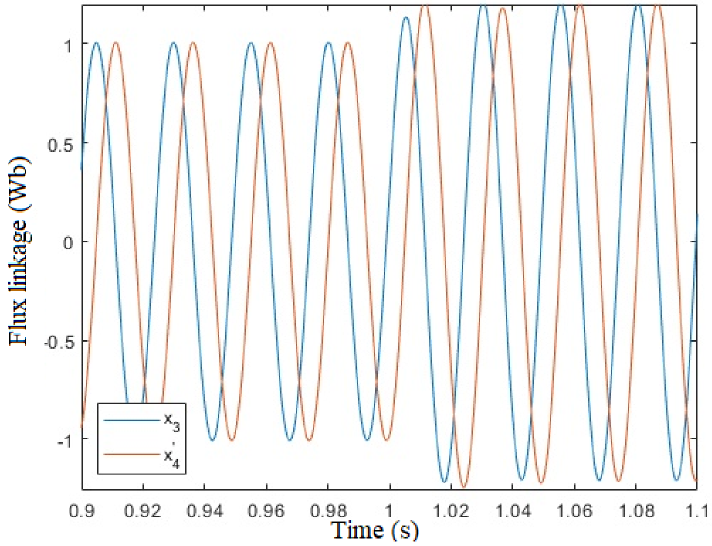

Figure 9. Measured λ_α and λ_β over time after a 20% step variation of amplitude

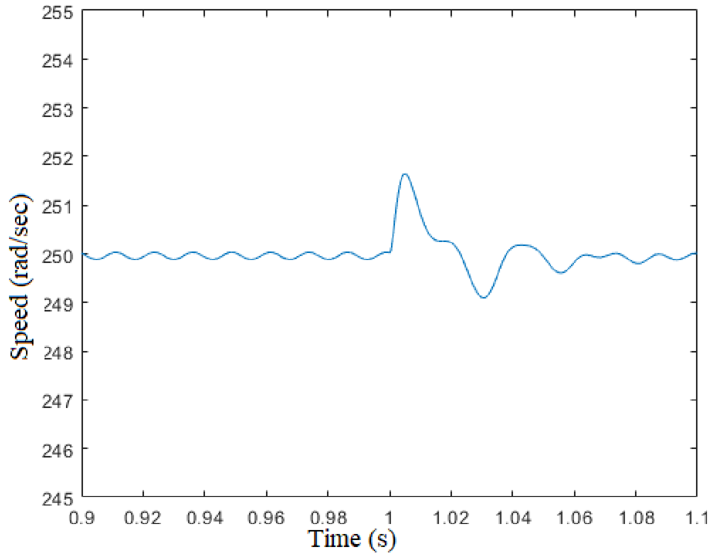

Figure 10. Measured ω_m^e over time after a 20% step variation of amplitude

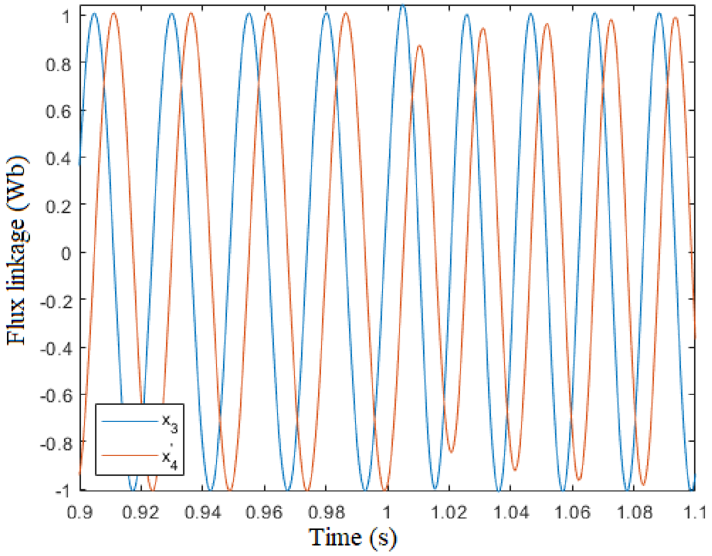

Figure 11. Measured λ_α and λ_β over time after a 20% step variation of frequency

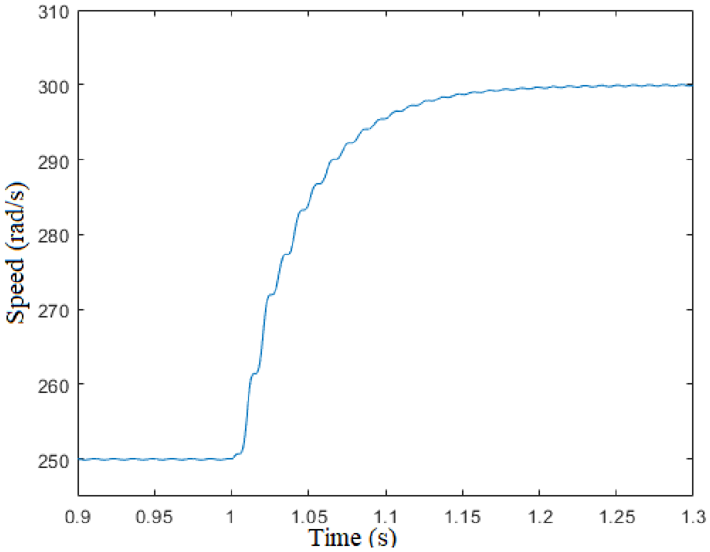

Figure 12. Measured ω_m^e over time after a 20% step variation of frequency

4.2. *Second Order - Second Order Generalized Integrator filtering*

In this section the filtering capabilites of the sensorless algotithm are described. Figure 13 and 14 show the Bode diagram of variable $x_3(s)$ and $x_4^{'}(s)$, mentioned in Figure 5 respectively. Figure 13 shows that the slope is -20dB/dec when $\omega \rightarrow 0$ and -60dB/dec when $\omega \rightarrow \infty$. Instead, Figure 14 shows that the slope is -40dB/dec when $\omega \rightarrow 0$ and -40dB/dec when $\omega \rightarrow \infty$. The DC gain in the results are almost and not perfectly 0 due to the sampling. In the center frequency the gain is 1 and at high frequency the attenuation is as expected by the Bode diagrams.

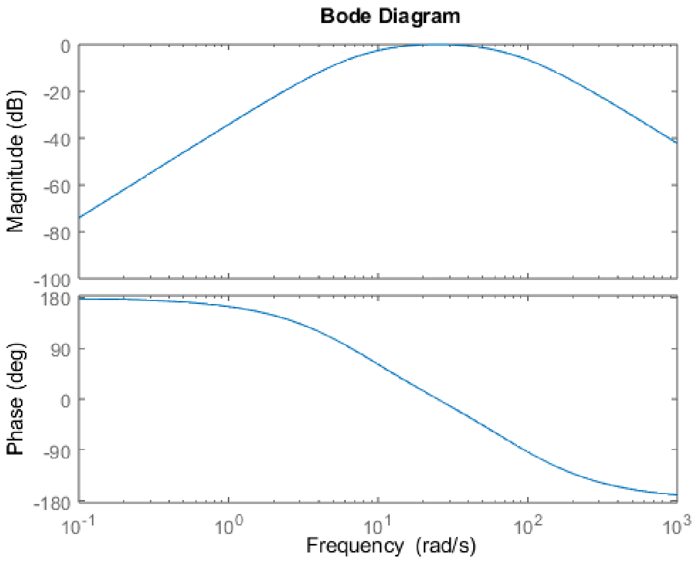

Figure 13. Bode diagram of $x_3(s)$

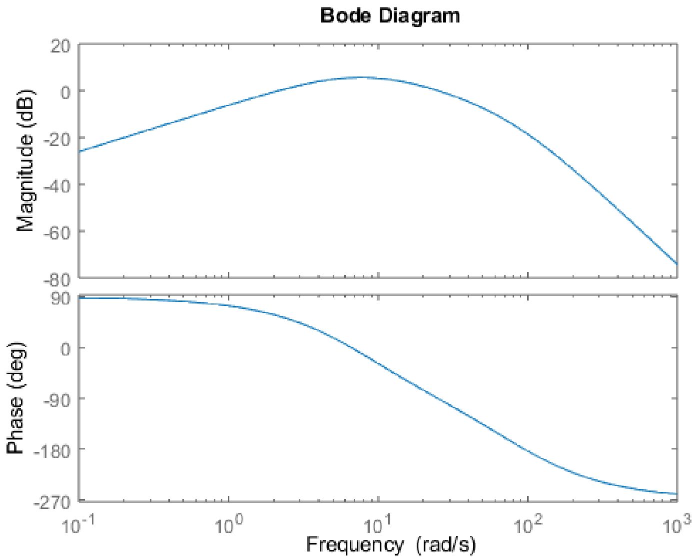

Figure 14. Bode diagram of $x_4'(s)$

4.3. *Quadrature Signal Generator - Phase Locked Loop*

The time response of the QSG-PLL has been set to $t_r = 0.1s$. This constrain leads the parameters of the PLL to be $k_p = 92$ and $k_i = 4232$. When the motor is accelerating, a static position error will appear while there will not be a static velocity error. That is because of applying a quadratic ramp to a Type two system. The static error can be calculated as a_e/k_i, where a_e is the electrical acceleration and k_i is the integral gain of the PI controller. Assuming a maximum mechanical acceleration of $a_m = 50rad/s$, which corresponds to electrical acceleration $a_e = 250rad/s$ the maximum error will be 0.0035 rad/s, that is negligible.

Figure 15 shows the time response of the estimated speed ω_m^e after a frequency step variation of 20%. The time response is about 100ms as designed.

Preprints.org (www.preprints.org) | NOT PEER-REVIEWED | Posted: 24 October 2024 doi:10.20944/preprints202410.1826.v1

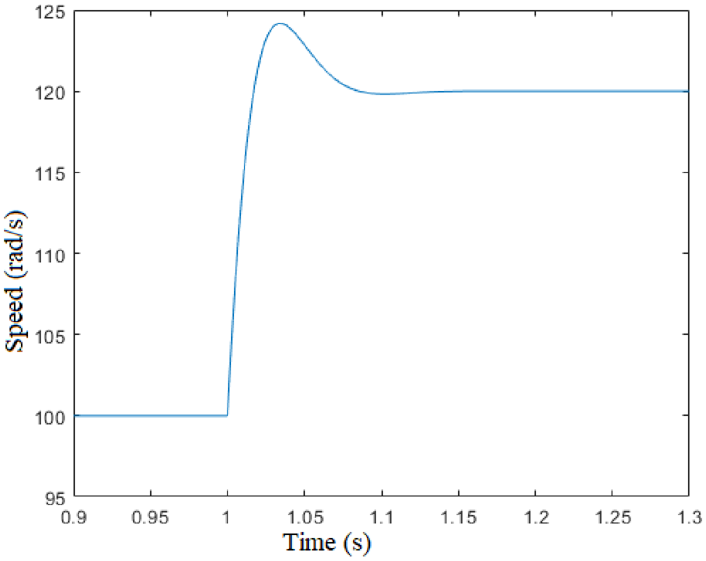

Figure 15. Measured ω_m^e over time

4.4. Steady-State

This section describes the steady-state performance of the sensorless algorithm at

1. low speed: $\omega_m^e = 25$ rad/s, which is about 47 rpm
2. medium speed: $\omega_m^e = 250$ rad/s, which is about 477 rpm

Figures 16–18 show the effect of the speed oscillation due to the cogging torque. Figure 18 and 19 show that the flux linkage $\lambda_{\alpha\beta}$ moves along a circle centered in (0,0), because the dc component of the α and β emf are effectively rejected. Figure 20 and 21 show the steady state angle error at low and medium speed. The maximum error of angle estimation is 0.25 rad when ω_m^e = 25 rad/s, and 0.12 rad when ω_m^e = 250 rad/s. One part of this error is due to the sampling delay. It can be estimated by $\Delta\theta_m^e = \omega_m^e T$ in the worst case, where T is the sampling delay which is 50μs, since $T = 1/f$ and $f = 20kHz$. At $\omega_m^e = 25$ rad/s the angular error due to the sampling delay is then $\Delta\theta_m^e = 0.0013$ rad, which is about 0.0074° and at $\omega_m^e = 250$ rad/s is about 0.013 rad/s, which is 0.074°. The error due to the sampling delay is then negligible at low and medium speed, and the main factor of the angle error is parameter mismatch.

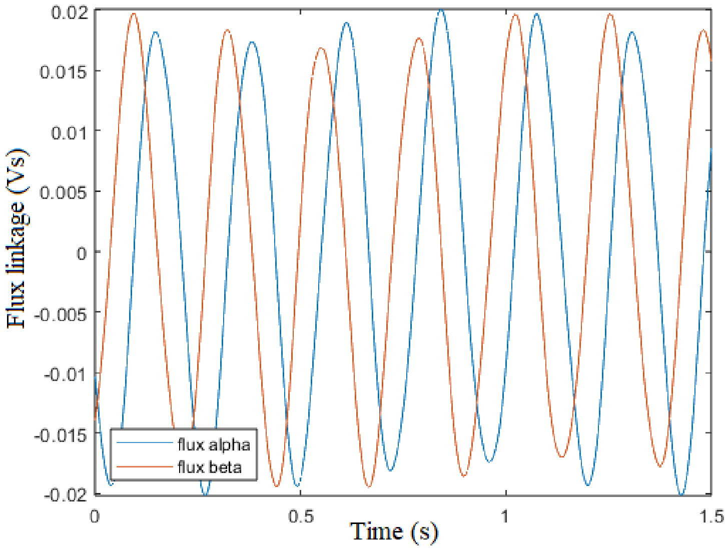

Figure 16. Measured λ_α and λ_β vs time (25 rad/s)

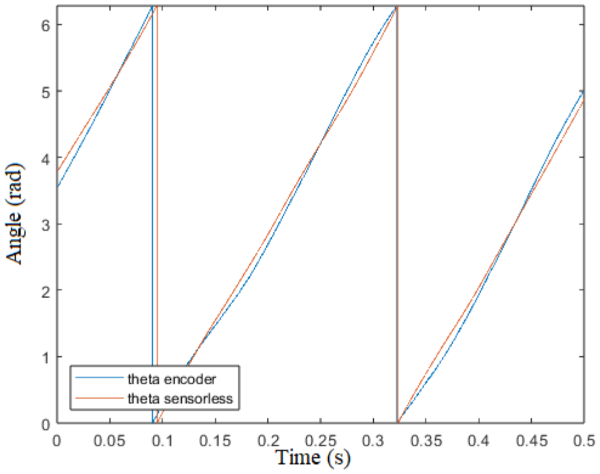

Figure 17. θ_m^e encoder and $\hat{\theta}_m^e$ sensorless vs time (25 rad/s)

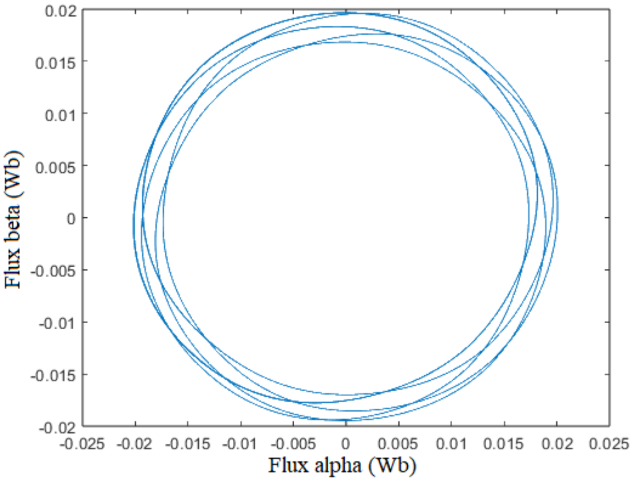

Figure 18. Measured λ_α vs λ_β (25 rad/s)

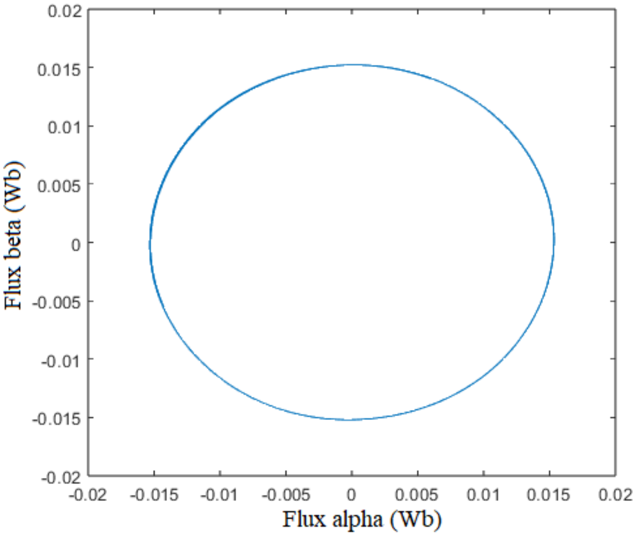

Figure 19. Measured λ_α vs λ_β (250 rad/s)

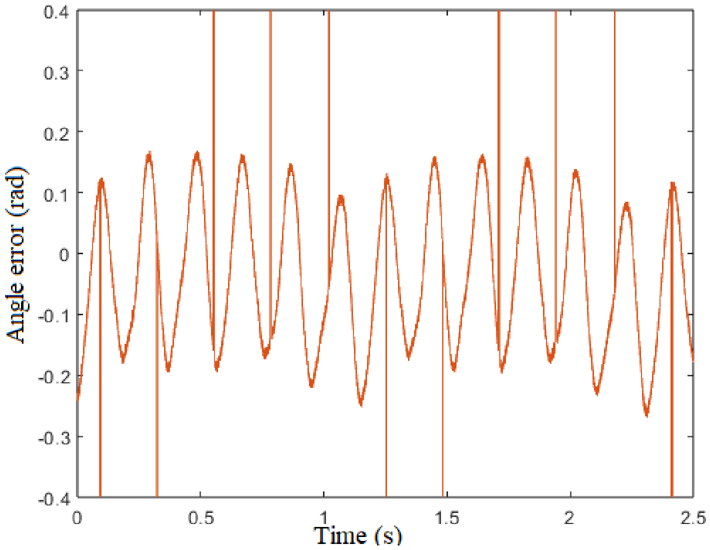

Figure 20. θ_m^e error vs time (25 rad/s)

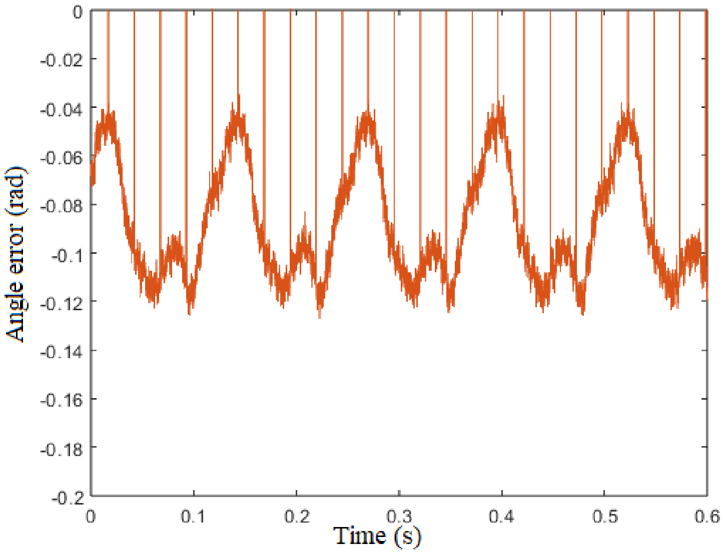

Figure 21. θ_m^e error vs time (250 rad/s)

4.5. Dynamic

This section deals with the performance of the sensorless algorithm during a variation of the speed reference and a variation of the load torque. Figure 22 and 23 show the results after a step variation of the ω_m^e reference from 100 to 200 rad/s and vice versa. The results show the stability of the sensorless algorithm even after a fast ω_m^e variation. The maximum angle error is $\Delta\theta_m^e = |0.7|rad$. Figure 24 and 25 show the results after a step load variation of the $+0.4Nm$ and vice versa. The results show the stability of the sensorless algorithm even after a fast torque variation. The maximum angle error is $\Delta\theta_m^e = |0.5|rad$.

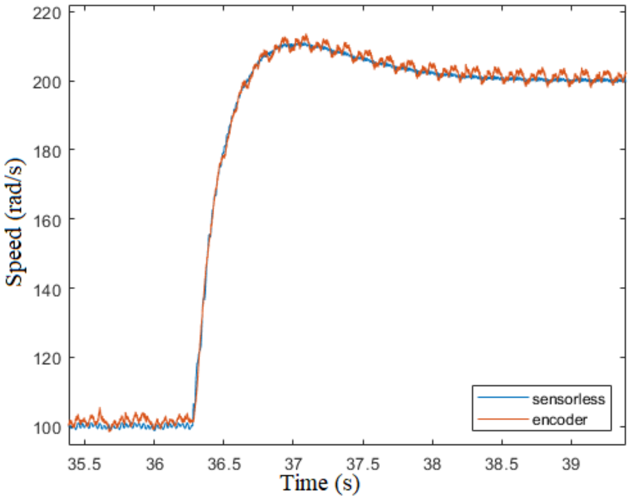

Figure 22. Actual and estimated speed behaviour after a reference speed variation from 100 to 200 rad/s.

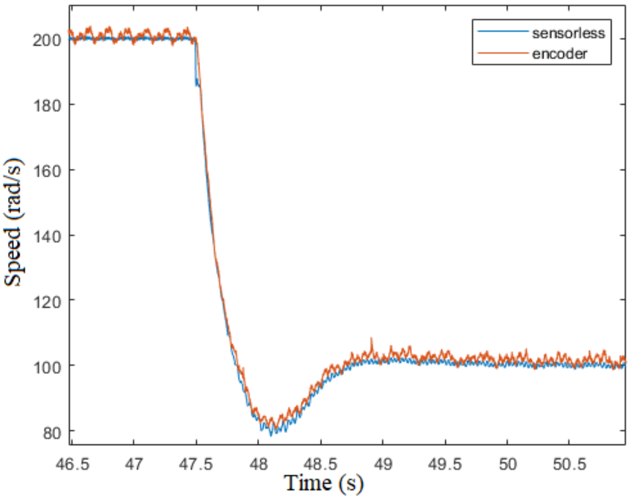

Figure 23. Actual and estimated speed behaviour after a reference speed variation from 200 to 100 rad/s.

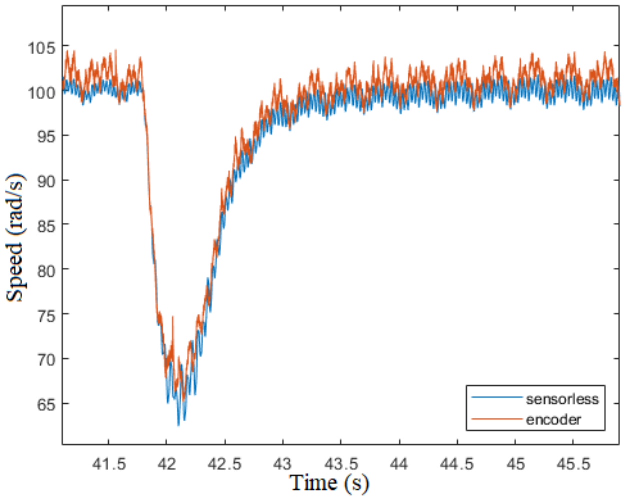

Figure 24. Actual and estimated speed behaviour after a step load variation of +0.4Nm.

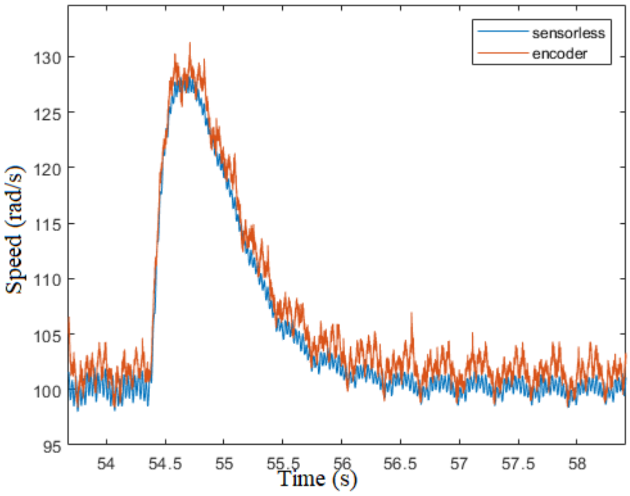

Figure 25. Actual and estimated speed behaviour after a step load variation of -0.4Nm.

5. Conclusions

In this paper, a sensorless algorithm is designed for a PM synchronous motor using an advanced second order-second order generalized integrator filter and a quadrature signal generator phase locked loop controller is used to estimate the rotor position from the filtered output.
The sensorless algorithm is initiated at 25 rad/s electrical angular frequency of the back-emf, that corresponds to 48rpm.

1. Low speed: $\omega_m^e = 25$ rad/s, approximately 48rpm
2. Medium speed: $\omega_m^e = 250$ rad/s, approximately 477rpm

A negligible error of 0.0035 rad is recorded at a maximum mechanical acceleration of $a_m = 50 rad/s$, with $v = A\cos(\omega t)$ as input of SO-SOGI, where $A = 1$ and $\omega_m^e = 250$ rad/s. The time response of the estimated speed $\hat{\omega}_m^e$ is approximately 100ms after a frequency step variation of 20%. In the steady-state performance of the sensorless algorithm, the maximum error in angle estimation is 0.25 rad at $\omega_m^e = 25$ rad/s, and 0.12 rad at $\omega_m^e = 250$ rad/s. Part of this error is due to the sampling delay. It can be estimated by $\Delta\theta_m^e = \omega_m^e T$ in the worst case, where T is the sampling delay of 50μs, given that $T = 1/f$ and $f = 20$kHz. At $\omega_m^e = 25$ rad/s, the angular error due to the sampling delay is $\Delta\theta_m^e = 0.0013$ rad, approximately 0.0074°, and at $\omega_m^e = 250$ rad/s, it is about 0.013 rad, or 0.074°. Thus, the error due to the sampling delay is negligible at both low and medium speeds. Stability of the motor during rapid variation of the reference speed and load torque shows the performance of the sensorless algorithm. The maximum angle error during a fast ω_m^e variation is $\Delta\theta_m^e = \pm 0.7$ rad. Similarly, the algorithm remains stable after rapid torque variations, with the maximum angle error of $\Delta\theta_m^e = \pm 0.5$ rad.

Author Contributions: Following are the authors contribution to this work: A.P. Formal analysis, investigation, data curation, editing and prepration of the final draft were caried out by Engr.Abdin pasund. P.F.S. The methodology, software and the validation were handled by Engr.Pier Francesco Sartori and the initial draft is prepared by P.F.S.; N.B.—The research concept was developed by professor Dr.Nicola bianchi, who also provided the necessary resources for the simulation and testing equipment. Dr.Bianchi served as the supervisor, reviewer and the editor of this article.

Acknowledgments: We are grateful to all the colleagues at the Electric Drive Laboratory (EDLAB) for their invaluable support in the preparation of this article.

Abbreviations

The following abbreviations are used in this manuscript:

EVs	Electric vehicles
PM	Permanet magnet
SPM	Surface mounted permanent magnet
FOC	Field oriented control
EMF	Electromotive force
SVM	Space vector modulation
SOIFO	Second-order integral flux observer
SO-SOGI	Second-order second-order generalized integral
PMSM	Permanent magnet synchronous motor
PI	Proportional integral
FLL	Frequency locked loop
PLL	Phase locked loop
QSG-PLL	Quadrature signal generated phase locked loop

References

1. Vagati, A.; Pellegrino, G.; Guglielmi, P. Comparison between SPM and IPM motor drives for EV application. In Proceedings of the The XIX International Conference on Electrical Machines - ICEM 2010, 2010, pp. 1–6.
2. Bianchi, N.; Bolognani, S.; Frare, P. Design criteria for high-efficiency SPM synchronous motors. *IEEE Transactions on Energy Conversion* **2006**, *21*, 396–404.
3. Vu, N.T.; Choi, H.H.; Kim, R.Y.; Jung, J.W. Robust speed control method for permanent magnet synchronous motor. *IET electric power applications* **2012**, *6*, 399–411.
4. Xin, Z.; Wang, X.; Qin, Z.; Lu, M.; Loh, P.C.; Blaabjerg, F. An improved second-order generalized integrator based quadrature signal generator. *IEEE Transactions on Power Electronics* **2016**, *31*, 8068–8073.
5. Mukherjee, P.; Paitandi, S.; Sengupta, M. Sensorless speed control of a laboratory fabricated SPM-BLDC motor prototype. *Sādhanā* **2023**, *48*, 236.
6. Sun, L.; Li, X.; Chen, L. Motor Speed Control With Convex Optimization-Based Position Estimation in the Current Loop. *IEEE Transactions on Power Electronics* **2021**, *36*, 10906–10919.
7. Xu, W.; Jiang, Y.; Mu, C.; Blaabjerg, F. Improved nonlinear flux observer-based second-order SOIFO for PMSM sensorless control. *IEEE Transactions on Power Electronics* **2018**, *34*, 565–579.
8. Jiang, Y.; Xu, W.; Mu, C. Improved SOIFO-based rotor flux observer for PMSM sensorless control. In Proceedings of the IECON 2017-43rd Annual Conference of the IEEE Industrial Electronics Society. IEEE, 2017, pp. 8219–8224.
9. Teodorescu, R.; Liserre, M.; Rodriguez, P. Grid synchronization in singlephase power converters **2007**.
10. Schenke, M.; Wallscheid, O. A deep Q-learning direct torque controller for permanent magnet synchronous motors. *IEEE Open Journal of the Industrial Electronics Society* **2021**, *2*, 388–400.
11. Öztürk, N.; Celik, E. Speed control of permanent magnet synchronous motors using fuzzy controller based on genetic algorithms. *International Journal of Electrical Power & Energy Systems* **2012**, *43*, 889–898.
12. Devi, G.R.; Rajambal, K. Novel space vector pulse width modulation technique for 5-Phase voltage source inverter. In Proceedings of the 2018 IEEE International Conference on System, Computation, Automation and Networking (ICSCA). IEEE, 2018, pp. 1–9.
13. Lee, Y.H.; Hsieh, M.F. Swiveling Magnetization for Anisotropic Magnets for Variable Flux Spoke-Type Permanent Magnet Motor Applied to Electric Vehicles. *Energies* **2022**, *15*, 3825.
14. Shen, H.; Luo, X.; Liang, G.; Shen, A. A robust dynamic decoupling control scheme for PMSM current loops based on improved sliding mode observer. *Journal of Power Electronics* **2018**, *18*, 1708–1719.
15. Song, Y.; Song, Z.; Yao, X. Permanent Magnet Synchronous Motor Control Based on New Sliding Mode Observer. In Proceedings of the Journal of Physics: Conference Series. IOP Publishing, 2022, Vol. 2218, p. 012058.

16. Huang, Y.; Tao, T.; Liu, Y.; Chen, K.; Yang, F. DSC-FLL based sensorless control for permanent magnet synchronous motor. *Progress In Electromagnetics Research M* **2020**, *98*, 171–181.
17. Zheng, Y.; Chang, Y.; Liu, D.; Wang, H.; Zuo, Y.; Ge, X. Sensorless Control of Permanent Magnet Synchronous Motor Based on Finite-Position-Set-Phase-Locked Loop. In Proceedings of the 2022 IEEE 5th International Electrical and Energy Conference (CIEEC). IEEE, 2022, pp. 2790–2795.